

# Evaluation of a Threshold-based Model of the Elevated-Temperature Fatigue of Impact-Damaged $\gamma$ -TiAl

TREVOR S. HARDING and J. WAYNE JONES

Step-loading fatigue tests have been conducted on two  $\gamma$ -TiAl alloys with differing microstructures following quasi-static indentations intended to simulate assembly-related impact damage to low-pressure turbine blades. Fatigue tests were conducted at 600 °C using computer-controlled servohydraulic loading at a frequency of 20 Hz. Reasonably good agreement was achieved between the fatigue data and calculated fatigue strength based on the fatigue threshold and measured impact severity. In certain cases, the fatigue threshold model fails to completely describe the data. These discrepancies may be related to residual stresses, variations in crack-shape morphology, and small-crack effects. Residual stresses could not be directly measured, given the small size of the damage zones. However, a comparison of fatigue threshold approximations based on a through-thickness crack geometry and a corner-crack geometry suggests that these two models may represent the upper and lower bounds of the actual fatigue behavior. In addition, the behavior of small cracks was examined by modeling the stress-lifetime response of lightly damaged specimens of the duplex alloy. This effort indicates the need for small-crack fatigue threshold values when designing fatigue-critical  $\gamma$ -TiAl components.

## I. INTRODUCTION

THE drive to reduce aircraft gas turbine engine weight, while improving performance and efficiency, has made  $\gamma$ -TiAl alloys candidates to replace current nickel-based superalloys as the material of choice for low-pressure turbine blades. This is primarily a result of the low density, high specific stiffness, elevated-temperature strength retention, and good environmental resistance of  $\gamma$ -TiAl. The lower density, in particular, will lead to significant engine weight savings and reduced stresses on rotating components such as low-pressure turbine blades.<sup>[1]</sup>

A significant drawback to  $\gamma$ -TiAl alloys, in terms of component design, is their limited fatigue-crack-growth resistance compared to nickel-based superalloys.<sup>[2,3]</sup> In general, there is a small difference between the fatigue threshold stress-intensity-range of long cracks and the apparent fracture toughness, leading to dramatically shortened lifetimes for small changes in applied stress, should the fatigue threshold be exceeded.<sup>[4-7]</sup> This is particularly problematic when extrinsic damage eliminates the need for initiation. Because of these factors, a damage-tolerant approach to design for  $\gamma$ -TiAl alloys may require the use of more-accurate crack detection methods and shorter inspection intervals, both of which add cost to engine operation. A preferable approach to designing with  $\gamma$ -TiAl is to use fatigue endurance limits and fatigue thresholds for determining acceptable operating stresses. This approach has the advantage of ensuring that components with pre-existing flaws will have a theoretically infinite life. In addition, this method reduces the effort at the design stage (*i.e.*, there is no need for lifetime summation over complex engine-loading spectra) and reduces the need for engine inspections.<sup>[1]</sup>

A serious limitation to a threshold-based design philosophy is that the anticipated size of any pre-existing flaws must be known accurately. In the case of assembly-related impacts or foreign-object damage (FOD), this may prove difficult. The effects of simulated FOD on fatigue properties have been examined for conventional titanium alloys, as well as  $\gamma$ -TiAl, but to date, none have examined impact damage in light of a threshold-based design approach.<sup>[8-11]</sup> The present study examines the effects of assembly-related (“shop floor”) impact damage on fatigue strength and uses a threshold-based model to predict this response over a range of damage severities. Particular issues such as small-crack effects and the shape of the initial damage have been examined and are discussed.

## II. MATERIALS AND EXPERIMENTAL PROCEDURE

### A. Materials and Specimens

In the present study, two different gamma titanium aluminum alloys were examined. The first of these, designated “48-2-2,”<sup>[12]</sup> had a nominal composition of Ti-47.9Al-2.0Cr-1.9Nb (at. pct). Plates were investment cast with final dimensions of 12.5 × 100 × 140 mm. These plates were first heat treated in vacuum at 1093 °C for 5 hours, followed by a hot isostatic press (HIP) at 1205 °C and 172 MPa for 4 hours. A final heat treatment of 1205 °C for 2 hours and a rapid cool completed the processing. The final microstructure, shown in Figure 1, consisted of a near- $\gamma$  structure of equiaxed gamma grains, roughly 70  $\mu$ m in diameter, with about 6.0 vol pct  $\gamma$ - $\alpha_2$  lamellar colonies. The  $\alpha_2$  phase was also observed along intergranular boundaries, as illustrated in the backscattered electron (BSE) image shown in Figure 2. The overall volume fraction of the  $\alpha_2$  phase present at both intergranular boundaries and in lamellar colonies was approximately 13 vol pct. The room-temperature properties of 48-2-2 include a yield strength of 330 MPa, ultimate tensile strength of 435 MPa, and tensile elongation of 1.8

TREVOR S. HARDING, Assistant Professor, is with the Manufacturing Engineering Department, Kettering University, Flint, MI 48504-4898. J. WAYNE JONES, Professor, is with the Department of Materials Science and Engineering, University of Michigan, Ann Arbor, MI 48109-2136.

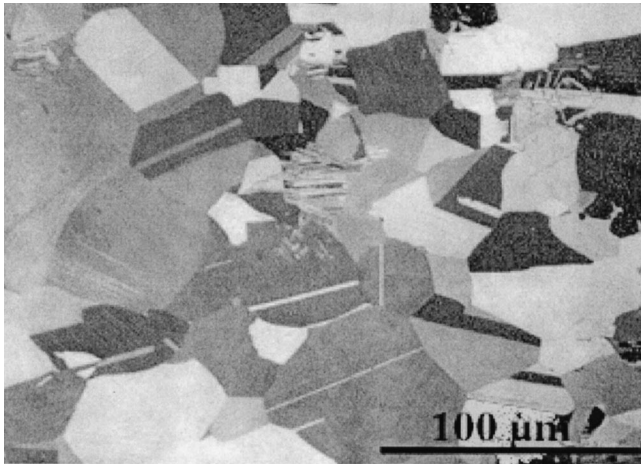


Fig. 1—Optical micrograph of duplex 48-2-2 alloy showing 70  $\mu\text{m}$  equiaxed  $\gamma$  grains and a small fraction of lamellar ( $\gamma$ - $\alpha_2$ ) colonies.

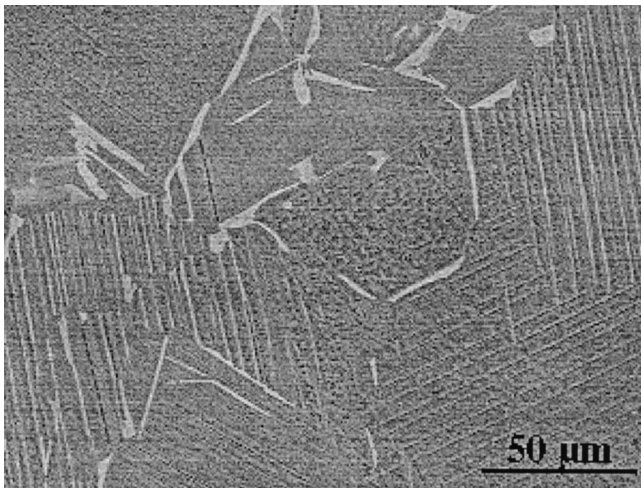


Fig. 2—BSE image of the duplex 48-2-2 microstructure with  $\alpha_2$  (light gray) phase along  $\gamma$  grain boundaries and within ( $\gamma$ - $\alpha_2$ ) lamellar colonies.

pct. These data were determined from specimens with an as-ground surface finish and using standard tensile testing procedures.<sup>[13]</sup>

The second alloy had a nominal composition of Ti-47.3Al-2.2Nb-0.5Mn-0.4W-0.4Mo-0.23Si (at. pct) and is referred to as “WMS.” The alloy was investment cast into plates with final dimensions of 12.5  $\times$  100  $\times$  150 mm. Processing included a HIP treatment of 1260  $^\circ\text{C}$  and 172 MPa for 4 hours, followed by a heat treatment of 1010  $^\circ\text{C}$  for 50 hours. The final microstructure produced by this processing is shown in Figure 3. Quantitative microscopy of specimens heat tinted at 600  $^\circ\text{C}$  revealed a duplex structure consisting of lamellar colonies, with equiaxed gamma grains at colony boundaries occupying about 25 pct of the microstructure. The lamellar colony size was on the order of 210  $\mu\text{m}$ , whereas the  $\gamma$  grain size was roughly 14  $\mu\text{m}$ . The BSE imaging revealed the presence of the ordered B2 phase along lamellar colony boundaries, as shown in Figure 4. The B2 volume fraction was approximately 2.0 vol pct. Room-temperature mechanical properties, determined from specimens with a chem-milled surface finish, include a yield strength of 503 MPa, ultimate tensile strength of 545 MPa, and tensile elongation of 0.5 pct.<sup>[14]</sup>

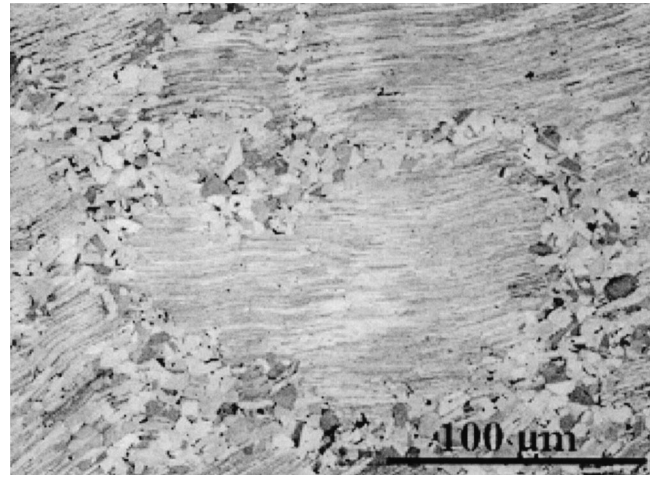


Fig. 3—Optical micrograph of the lamellar WMS alloy revealing lamellar colonies of roughly 210  $\mu\text{m}$  in diameter surrounded by small equiaxed gamma grains.

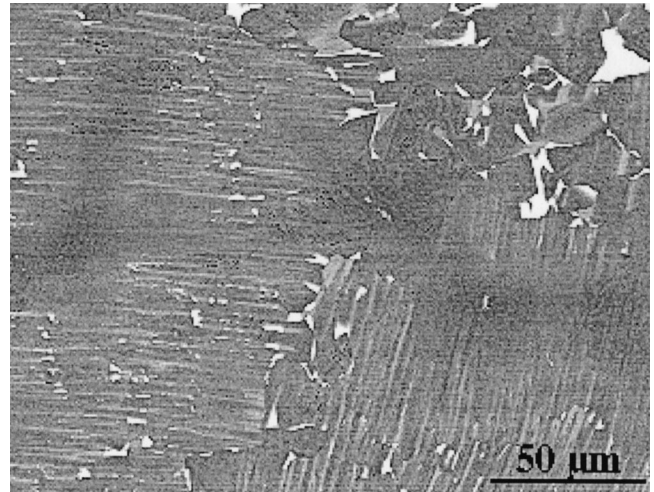


Fig. 4—BSE image of lamellar WMS alloy showing the existence of the B2 phase (white spots) at colony boundaries.

Cast plates for both alloys were electro-discharge machined (EDM) into blanks and low-stress ground to the desired nominal dimensions. Fatigue specimens were 136-mm long with a gage section that was 3  $\times$  6 mm. Machining was followed by a hand grinding procedure until a surface finish equivalent to 600 grit was achieved. Each specimen was then electropolished in a solution of 60 pct methanol, 35 pct *n*-butanol, and 5 pct perchloric acid (by volume) at  $-50$   $^\circ\text{C}$  and 25 V.

### B. Impact Damage

Simulated impact damage was introduced into the specimens by a quasi-static indentation process. A screw-driven mechanical testing machine was used to indent the 3-mm-thick side of the specimen with a hardened steel wedge, as shown schematically in Figure 5. The wedge had a flank angle of 60 deg, and all indents were conducted at room temperature. The loads introduced into the specimen during indentation were monitored using a load cell. These data

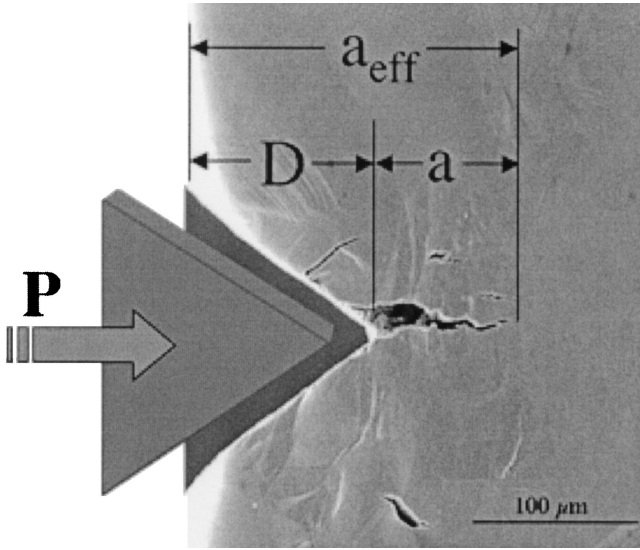


Fig. 5—Schematic drawing of impact damage parameters: peak impact load ( $P$ ), indent depth ( $D$ ), indent-tip crack length ( $a$ ), and effective crack length ( $a_{\text{eff}}$ ).

were then used to determine the peak load of indentation. Although quasi-static indents occur at speeds far lower than what might be expected for assembly-related damage, this method was found to give highly repeatable damage levels for a given peak load. Earlier experiments with a drop-weight impacting apparatus proved difficult to control and introduced more scatter in the impact-damage results. Furthermore, the loading rate appears to have little effect on the damage mechanism in  $\gamma$ -TiAl, which has been confirmed in tensile tests on similar alloys.<sup>[15,16]</sup>

Damage from the simulated impacts was defined in terms of critical parameters that were expected to play a significant role in subsequent fatigue properties. These parameters, all measured on the specimen surface and shown schematically in Figure 5, include the depth of the indent, length and position of cracks ahead of the indent, and the indent-tip radius. The indent depth ( $D$ ) and indent-tip radius ( $\rho$ ) for every impact site were measured. The final indent depth is taken as the average of the surface measurements made on both faces of the specimen. The indent-tip crack length ( $a$ ) is defined as the projected crack length from the indent tip to the tip of the crack. The length of the indent-tip crack is also averaged over both sides of the specimen. The effective crack length ( $a_{\text{eff}}$ ) is defined as the sum of the indent depth and the indent-tip crack length ( $a_{\text{eff}} = a + D$ ).

Scanning electron microscopy (SEM) was used to examine the fracture surfaces of specimens following fatigue testing. Information regarding impact damage and fatigue-crack propagation mechanisms was noted. In addition, a combination of SEM and optical techniques was used to map the shape of the initial impact damage and fatigue-crack-growth regions of fracture surfaces.

### C. Fatigue Tests

Fatigue tests were conducted on a closed-loop servo-hydraulic mechanical testing machine at 600 °C in air. Tests were run at a frequency of 20 Hz with a load ratio of  $R = 0.1$ . The specimens were heated using a four-zone quartz-lamp

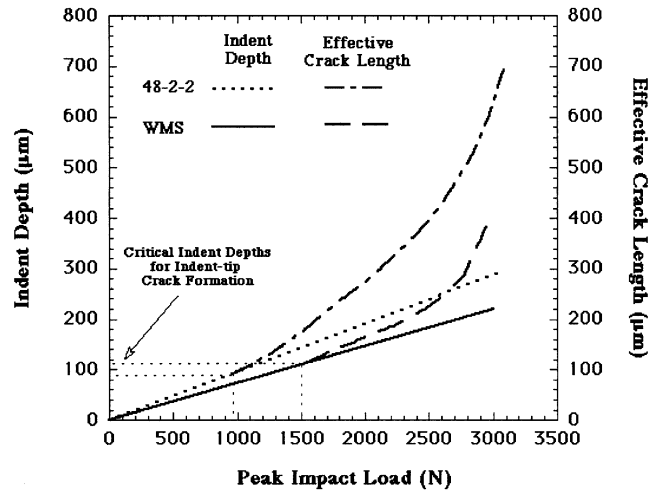


Fig. 6—Trend lines for impact damage in terms of indent depth and effective crack length with increasing damage severity (peak load) for both the 48-2-2 and WMS alloy. All damage was introduced at room temperature.

furnace. The specimen temperature was maintained at  $\pm 2$  °C in the damage zone. Fatigue strengths were measured using the step-test method, a step-loading fatigue test intended to determine the endurance limit of a material with a minimum of specimens.<sup>[17]</sup> The step test was necessary for developing fatigue-strength data over the wide range of peak loads and damage levels investigated in this study. Fatigue tests were begun at a stress amplitude of roughly 75 pct of the threshold stress, as determined from linear elastic fracture mechanics. This calculation used long-crack threshold data and the measured effective crack length. The maximum number of cycles in this first cycle block was  $10^5$  cycles. If the specimen survived this first cycle block, which occurred for every specimen examined, the maximum cyclic stress was increased by 10 MPa while the load ratio ( $R = \sigma_{\text{min}}/\sigma_{\text{max}}$ ) was held constant. Testing continued for yet another cycle block of  $10^5$  cycles, followed by more incremental stress increases until specimen failure. The fatigue failure stress was defined as the highest stress level at which a specimen was able to survive a full  $10^5$  cycle block. Given the flatness of the stress-lifetime curves of many  $\gamma$ -TiAl alloys,<sup>[16,18]</sup> the fatigue failure stress is considered a reasonable approximation of the endurance limit of the damaged specimen.

## III. RESULTS AND DISCUSSION

### A. Impact Damage

Figure 6 illustrates schematically the observed trends in impact damage with increasing impact severity, or peak load. The depth of the indentation varies linearly with the peak load, for both the 48-2-2 and WMS alloys. Furthermore, the indent depth at a given peak load is higher for the 48-2-2 alloy than for the WMS alloy. This is likely a result of the higher yield strength of the WMS alloy. The relationship between peak impact load and indent depth was discussed further in a previous work.<sup>[19]</sup>

The formation of cracks at the indent tip occurred only when the peak load had reached a critical level, approximately 1000 and 1550 N for the 48-2-2 and WMS alloys, respectively, although some variability did exist. However,

on average, the indent depths associated with the critical peak loads were nearly the same for 48-2-2 and WMS, as shown in Figure 6, reflecting the significant difference in yield strength between the two alloys.

The formation of a crack at the tip of an indent is likely to be dependent on achieving a critical strain ahead of the indent, possibly related to tensile ductility. Some work has been conducted on the initiation of cracks at impact sites in  $\gamma$ -TiAl, which has shown that the extent of plastic strain in the vicinity of the impact site has a significant influence on crack initiation. Finite-element analyses of small-particle, ballistic impacts on turbine blade-shaped specimens found that the strains produced within the zone of cracking were close to the tensile ductility of the TiAl alloy under investigation (0.5 to 1.5 pct).<sup>[20]</sup> While the geometry is certainly not the same, these results point to the important role of tensile ductility in determining the extent of cracking which may occur in an impact event. Establishing the degree to which ductility controls this process would be difficult given the general variability in the ductility of gamma TiAl, as well as the inhomogeneity of the microstructure.

The variability in the impact load at which cracks initiate ahead of the indent is likely to be related to variations in local grain orientation at the indent tip. A study on notched gamma TiAl specimens under static loading found that cracks initiated within highly strained equiaxed  $\gamma$  grains or along grain boundaries that were preferably oriented for slip-line impingement, despite the fact that applied tensile stresses were well below the general yield.<sup>[21]</sup> Similar evidence of the significance of the local microstructure was seen in the specimens examined here in the form of intergranular cracks, which had initiated between two heavily strained grains with different orientations, and transgranular cracks, which had initiated and propagated along particularly heavy slip lines within grains.

An additional requirement must be met that the distance over which the critical strain is exceeded must be greater than a critical length parameter for crack initiation, possibly related to the microstructural scale. Since the size of the near-indent-tip strain field scales with the indent depth,<sup>[22]</sup> it is reasonable to suggest that the higher-yield-strength WMS alloy would provide greater resistance to the formation of cracks ahead of indents produced by a given impact event, as is observed.

The size of indent-tip cracks, based on measurements at the specimen surface, follows the same increasing trend in both alloys, although cracks in 48-2-2 will be significantly larger for a given peak load. The length of the crack will at first be determined by the size of the strain-field distribution where the strain exceeds the critical strain parameter.<sup>[19]</sup> However, as the indenter continues to be forced into the specimen, it will wedge open the crack mouth, increasing the crack-tip stress intensity and leading to further crack extension if the material toughness is exceeded at the crack tip. The lamellar microstructure of the WMS alloy provides greater apparent toughness and, hence, resistance to further growth of indent-tip cracks. This can be attributed to the more tortuous crack path observed in the indent-tip region of indented WMS specimens, which is a result of the variation in lamellae orientation<sup>[23–26]</sup> and of a greater propensity for shear ligament formation.<sup>[27,28]</sup> While these general trends indicate that the WMS alloy has a greater resistance to

impact damage, it should also be pointed out that the local microstructure can have an important influence as well. The presence of suitably oriented lamellar colonies near the indent tip has been observed to result in the extension of indent-tip cracks to lengths greater than those predicted by the trend lines in Figure 6.

Fractography using both SEM and optical microscopy was employed to quantitatively measure the extent of impact damage and subsequent fatigue-crack growth. The purpose of the examination was to more accurately estimate the size and morphology of cracks produced by damage and subsequent fatigue cycling. In general, cracks at the indent tip take on one of three morphologies, as shown schematically in Figure 7. For moderately and severely impacted specimens of the 48-2-2 alloy (Figures 7(a) and (b), respectively), cracking exists at the specimen surface, but is significantly reduced, or nonexistent, along the indent tip. In lightly damaged specimens (Figure 7(c)), where no cracking is observed on the specimen surface, small semielliptical cracks are frequently observed along the indent tip. For the WMS specimens, no examples of completely through-thickness cracks ahead of the indent tip, similar to the severely damaged specimen shown in Figure 7(c), were observed. Instead, all WMS specimens where surface cracking was clearly identifiable after indentation exhibited damage similar to that shown in Figure 7(b).

Regardless of the material or degree of damage severity, fatigue cracks were observed to propagate from the region along the indent tip where the initial damage was most severe (*i.e.*, of greatest length). This generally meant that in the case of severely and moderately damaged specimens, fatigue cracks grew as quarter-elliptical corner cracks. In lightly damaged specimens, fatigue cracks propagated as semielliptical surface cracks from the indent tip.

Our examinations of crack shape indicate clearly that cracks created by the indentation event are not easily, nor completely, characterized as through-thickness cracks. However, for the purposes of the threshold-based fatigue-life predictions that are analyzed in this article, we make the assumption that damage can indeed be characterized by through-thickness cracks. We do this for two reasons: (1) the effective crack length is comprised of a complex combination of a through-thickness sharp notch (indent) and true cracks extending from the notch tip, and (2) in practice, designers will rely on conservative estimates of crack shape and size to allow for the inaccuracies in inspection. Our previous work has shown that the indentations produced by the simulated impacts are sufficiently sharp to approximate actual cracks.<sup>[19]</sup> The errors associated with crack shape at the tip of the indents will, in all likelihood, be small, or at least no larger than those introduced by the influence of other geometrical and microstructural factors.

## B. Fatigue and Damage Tolerance

The reduction in the 600 °C fatigue strength, determined from step tests following the introduction of simulated impact damage, is shown in Figure 8 as a function of the peak load of the indentation. The room-temperature fatigue strengths of damaged specimens, which were previously reported, are shown for comparison.<sup>[29]</sup> Typical of  $\gamma$ -TiAl alloys, both 48-2-2 and WMS exhibit substantial strength retention at this elevated temperature, particularly at the

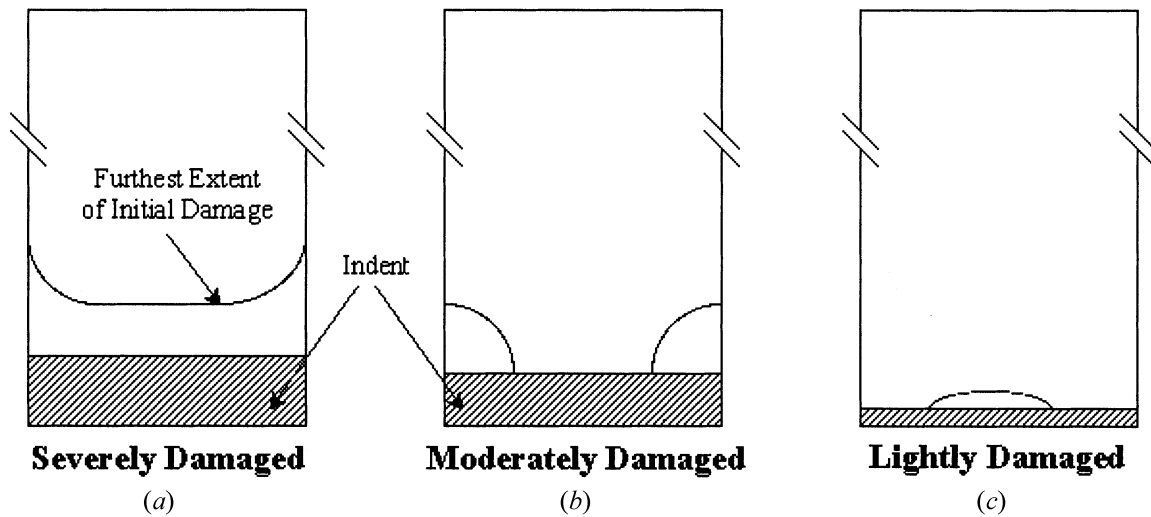


Fig. 7— (a) through (c) Schematic representation of the types of initial damage observed on the fracture surfaces of damaged specimens in the 48-2-2 and WMS alloys.

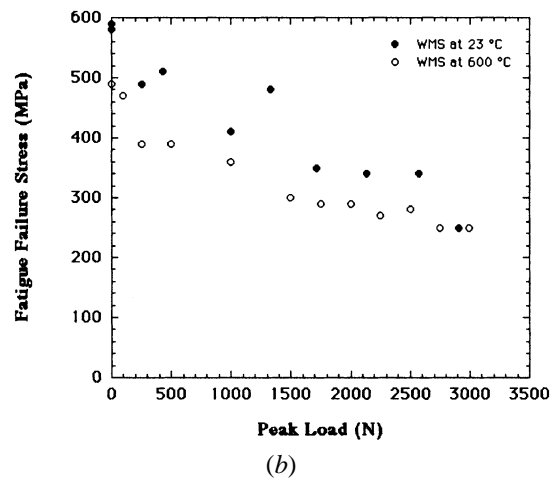
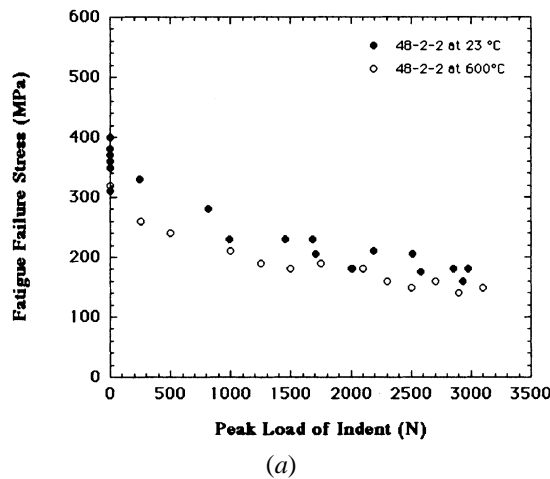


Fig. 8—The reduction in fatigue strength with peak load of indentation at 23 °C and 600 °C in the (a) duplex 48-2-2 alloy and (b) near fully lamellar WMS alloy. Both materials retain much of their strength at 600 °C, particularly at high impact severities.

most severe impacts.<sup>[16,30]</sup> The fatigue strength of the WMS alloy is higher than that of the 48-2-2 alloy at all temperatures

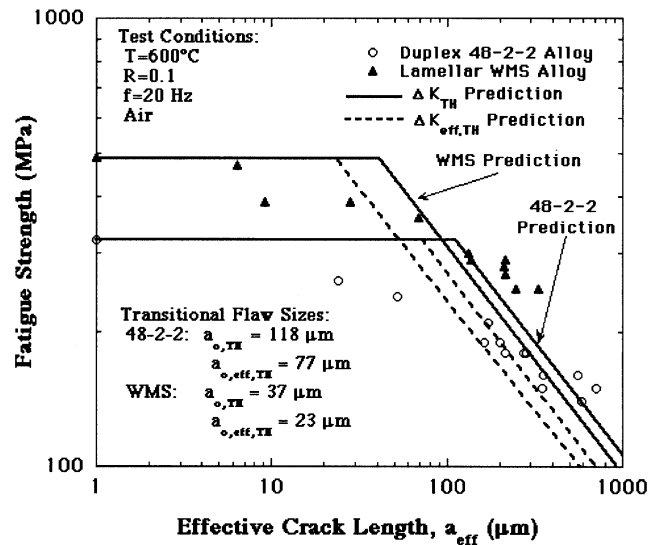


Fig. 9—Modified Kitagawa plot of 48-2-2 and WMS showing the reduction in fatigue strength as a function of effective crack length at 600 °C.

and peak loads. In the 48-2-2 alloy, the fatigue strength at 600 °C for undamaged specimens is 310 MPa compared to an average of  $360 \pm 80$  MPa at 23 °C. At 600 °C, the fatigue strength of undamaged WMS was found to be 495 MPa, compared to  $590 \pm 21$  MPa at 23 °C. The same decreasing trend in fatigue strength with increasing peak load is observed in the WMS alloy. The scatter observed in the room-temperature fatigue results is similar to that frequently observed in other  $\gamma$ -TiAl alloys.<sup>[31]</sup> Due to limited material, only two undamaged specimens were tested at 600 °C for both 48-2-2 and WMS, with no measured variation in fatigue failure stress between these two specimens.

For impact-damaged specimens, the fatigue strength was correlated with effective crack length using a modified form of the Kitagawa plot,<sup>[32]</sup> as shown in Figure 9. Solid lines in the figure represent the fatigue strength of undamaged material (slope = 0) and the threshold stress determined from a long-crack threshold-based approximation (slope =  $-1/2$ ).

The dashed line represents a threshold-based approximation determined from closure-corrected effective threshold stress-intensity-range data.

The threshold-based model of fatigue-strength prediction examined here and in earlier studies<sup>[29,33]</sup> is based on three assumptions:

- (1) Indent-tip cracks are assumed to be through-thickness and have a well-defined, uniform crack front.
- (2) When no indent-tip cracks are observed on the specimen surface, no cracks are assumed to have formed at any point along the indent tip.
- (3) Fatigue cracks are assumed to propagate from the indent-tip crack as through-thickness cracks.

The threshold-based approximation of fatigue strength is based on a linear elastic fracture-mechanics equation of the form

$$\sigma_{TH,max} = \frac{\Delta K_{TH}}{F(1-R)\sqrt{\pi a_{eff}}} \quad [1]$$

where  $\sigma_{TH,max}$  is the fatigue failure stress;  $F$  is the geometry correction factor for a through-thickness, single-edge crack;<sup>[34]</sup>  $R$  is the load ratio;  $\Delta K_{TH}$  is the long-crack threshold stress-intensity range; and  $a_{eff}$  is the effective crack length. A similar equation can be developed using the effective threshold stress-intensity range:

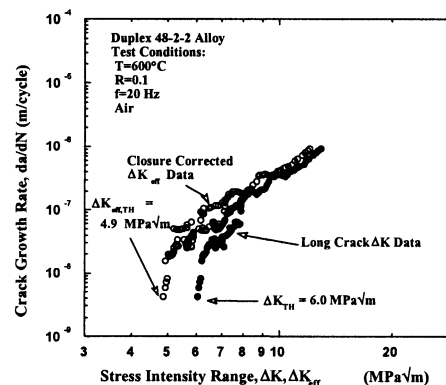
$$\sigma_{eff,TH,max} = \frac{\Delta K_{eff,TH}}{F(1-R)\sqrt{\pi a_{eff}}} \quad [2]$$

Values for  $\Delta K_{TH}$  and  $\Delta K_{eff,TH}$  were determined from the long-crack fatigue-crack growth-rate data shown in Figure 10.<sup>[14,35]</sup> At 600 °C, the duplex 48-2-2 alloy exhibits higher  $\Delta K_{TH}$  and  $\Delta K_{eff,TH}$  values than the lamellar WMS alloy, which exhibits an arrest-like near-threshold response and higher apparent toughness.

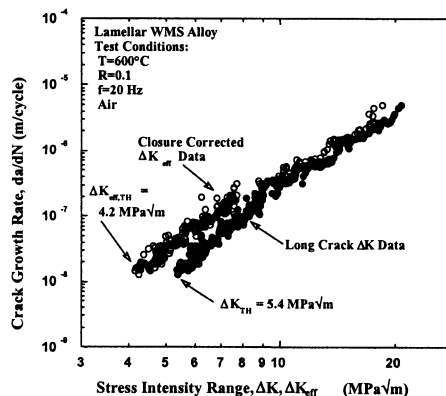
Figure 9 shows that the threshold-based approximation provides a reasonably good estimate of the fatigue strength in both the 48-2-2 and WMS alloys. However, the model does not accurately portray the behavior of damaged specimens at all crack sizes. This manifests itself in the form of conservative estimates of fatigue strength at large crack sizes and nonconservative estimates at small and intermediate crack sizes.

At large effective crack lengths, comparison of the threshold prediction lines in Figure 9 indicates that at equivalent damage levels, the WMS alloy would have a slightly lower predicted fatigue strength than that of the 48-2-2 alloy. From a design perspective based solely on threshold criteria, the 48-2-2 alloy would be a preferable choice for a given level of damage despite a lower fatigue strength in the undamaged condition. To the contrary, however, our experimental results indicate that the WMS alloy has a greater actual fatigue strength.

The differences between the measured fatigue strengths of damaged specimens and the threshold-based approximation, presented as a modified Kitagawa plot, may arise from several mechanisms. The irregular indent-tip crack fronts observed in the damage zone could lead to variations in the actual crack threshold compared to those values determined from specimens with precracks using a load-shedding technique.<sup>[14,35]</sup> Nor does the threshold model described here take into account any effects of residual stresses that may



(a)



(b)

Fig. 10—Crack growth rates for (a) the duplex 48-2-2 alloy and (b) the near-lamellar WMS alloy as determined at 600 °C.

exist in the indent plastic zone. Due to the small size of the damage zones and the steep residual stress gradients expected, it was not possible to directly measure residual stresses with available equipment. The assumption of a through-thickness crack geometry, as described previously, also certainly influences the accuracy of the threshold-based model; however, this assumption provides the most conservative results.

The nonconservative estimate of fatigue strength at small and intermediate crack sizes is attributed to a small-crack effect, which is commonly encountered in a Kitagawa approach.<sup>[36,37]</sup> Despite these potential sources of error in the model, it is encouraging to see how accurately the threshold-based model presented here predicts the fatigue strength of impact-damaged specimens.

### C. Examination of Behavior at Small-Crack Sizes in the 48-2-2 Alloy

As discussed previously, the measured fatigue strengths of small to intermediate effective crack lengths in both the 48-2-2 and WMS alloys are lower than that predicted by the threshold-based model or the fatigue strength of undamaged material. A likely explanation for this behavior is that below a certain crack size, the apparent threshold stress-intensity range diminishes with decreasing crack size, as demonstrated by Kitagawa and Takahashi in HT-80 steel.<sup>[32]</sup> Such behavior has been identified with small-crack growth, either through

a loss of closure or through a dependence of fatigue-crack growth on noncontinuum microstructural factors.

The need for a small-crack threshold for the design of fatigue-critical components using  $\gamma$ -TiAl can be realized by determining the transitional flaw sizes ( $a_{o,TH}$  and  $a_{o,eff,TH}$ ) which theoretically represent the length scale at which fatigue behavior transitions from being stress-dependent to threshold-dependent. The transitional flaw size is defined as the intersection of the line representing the fatigue strength and the threshold-based or effective threshold-based lines in a Kitagawa plot. Specific values for 48-2-2 and WMS are shown in Figure 9. Theoretically, the transitional flaw size defines the lower limit of the applicability of constant  $\Delta K_{TH}$  or  $\Delta K_{eff,TH}$  values,<sup>[32]</sup> which is important design information. However, as Figure 9 shows, cracks larger than  $a_{o,TH}$  can still lead to reductions in fatigue strength much greater than those predicted using either  $\Delta K_{TH}$  or  $\Delta K_{eff,TH}$ , suggesting that even at such large crack sizes, a small-crack threshold may be necessary.

A more meaningful parameter of the small-crack-to-long-crack transition may be the minimum flaw size at which the experimental fatigue data and the threshold-based prediction lines are in agreement, or the “critical crack length,” as it is sometimes referred to. In the 48-2-2 alloy, the critical crack length is approximately 570  $\mu\text{m}$ , roughly equivalent to eight equiaxed  $\gamma$  grains, which is in agreement with findings of other researchers in terms of a correlation with the primary microstructural feature size.<sup>[38]</sup> In the WMS alloy, clear definition of a correlation between the critical crack size and microstructure is more difficult. The critical crack length is roughly 80  $\mu\text{m}$ , while the average lamellar colony size is 210  $\mu\text{m}$ . Similar difficulties in defining transitional flaw sizes for small-crack behavior in lamellar alloys has been encountered in other  $\gamma$ -TiAl alloys.<sup>[39]</sup> However, seeing that WMS is a duplex alloy, one could argue that it may, in fact, be the equiaxed gamma grain size which controls the magnitude of critical or transitional crack sizes. In WMS, the critical crack length is approximately 5 to 6 times larger than the equiaxed  $\gamma$  grains, which is close to the relationship observed in the 48-2-2 alloy. For duplex alloys, the relative significance of the equiaxed gamma grain size and lamellar colony size on the behavior of small cracks in  $\gamma$ -TiAl is as yet unclear.

Regardless of the transitional flaw size used, the influence of flaw size is an important one for any threshold-based approach to predicting fatigue strength. To examine the change in fatigue threshold as a function of crack size, standard constant-amplitude fatigue tests were conducted on damaged 48-2-2 specimens at 600 °C. The WMS alloy was not included in this investigation due to a lack of material. Five 48-2-2 specimens were indented at 1000 N to produce effective crack lengths less than 100  $\mu\text{m}$ . Five additional specimens were damaged at 3000 N to produce effective cracks larger than 500  $\mu\text{m}$ . Figure 11 shows the results of the constant-amplitude fatigue tests. The difference in fatigue strength between finite lifetimes and a run-out at  $10^7$  cycles is small. Such behavior has been reported for undamaged specimens of other  $\gamma$ -TiAl alloys by Dolley *et al.*<sup>[18]</sup> and Trail and Bowen<sup>[31]</sup> and is a result of the small difference between  $\Delta K_{TH}$  and the apparent toughness. Figure 11 also demonstrates that impact damage can lead to a significant decrease in fatigue strength. The fatigue strength at  $10^5$

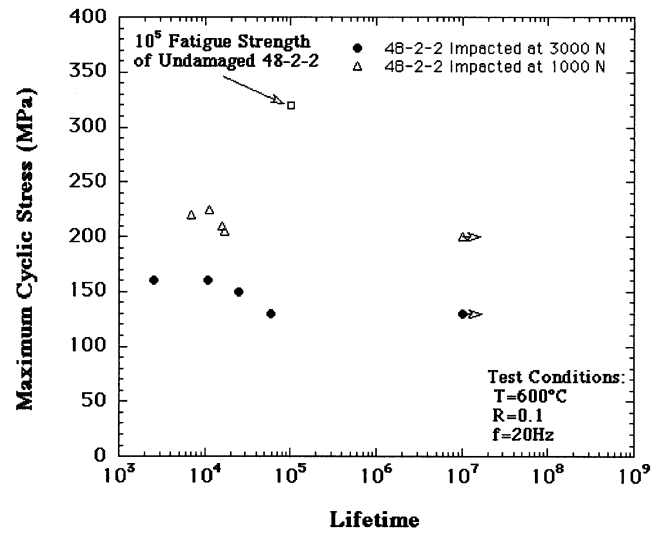


Fig. 11—Results of constant amplitude stress fatigue tests at 600 °C for specimens of the 48-2-2 alloy impacted at 1000 and 3000 N.

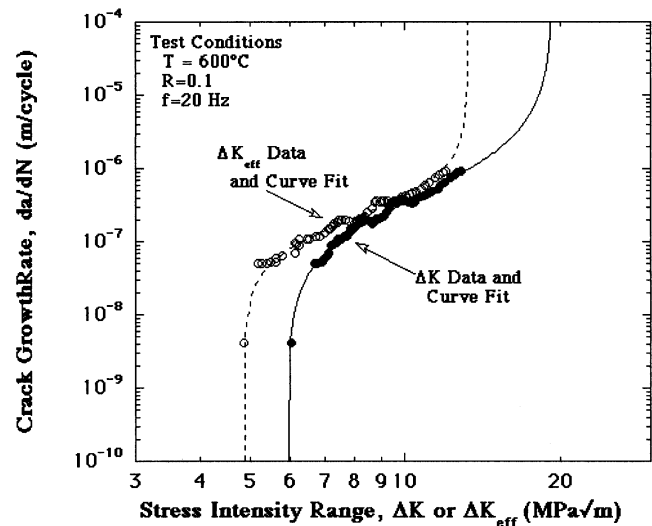


Fig. 12—Regression of 600 °C fatigue crack growth data of the duplex 48-2-2 alloy using the ATANH equation.

cycles for the undamaged material was found to be 320 MPa using the step-test method. In comparison, specimens indented at a peak load of 3000 N had an endurance limit of only 130 MPa, as determined from standard constant-amplitude tests. Likewise, indents of 1000 N resulted in a measured endurance limit of 200 MPa.

Examination of the small-crack effect in 48-2-2 was accomplished by modeling the stress-lifetime response of specimens tested in the constant-amplitude tests with a long-crack fatigue-crack-growth equation, discussed in more detail by Larsen *et al.*<sup>[40]</sup> The governing equation, referred to as the ATANH equation, has the form

$$\log (da/dN) = C_1 \arctan h (C_2 (\log (\Delta K) + C_3)) + C_4 \quad [3]$$

where  $C_1$  through  $C_4$  are constants dependent on the material and test conditions and are determined by regression of the crack-growth data shown in Figure 10(a). As Figure 12

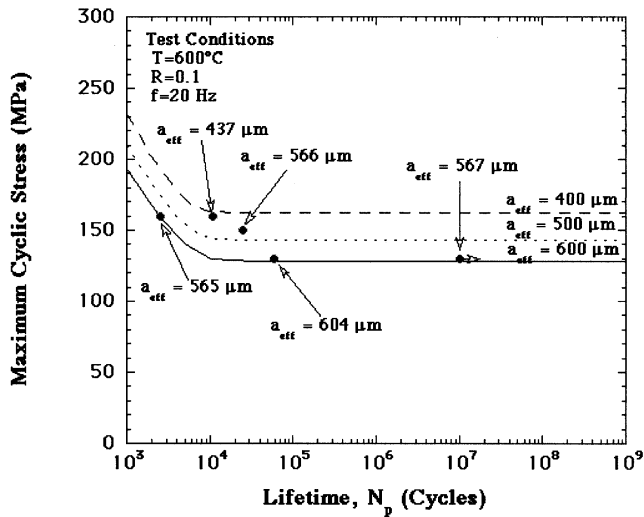


Fig. 13—Comparison of stress-lifetime response of 48-2-2 specimens impacted at 3000 N and tested at 600 °C with the curves generated from the ATANH equation using  $\Delta K_{TH}$  data, which bound the measured stress-lifetime response of these long cracks closely. The initial effective crack lengths of each specimen are shown for comparison.

illustrates, the asymptotic nature of Eq. [3] accurately portrays the near-threshold fatigue behavior of the 48-2-2 alloy for both  $\Delta K$  and  $\Delta K_{eff}$ .

The stress-lifetime response of the impacted 48-2-2 specimens can be estimated by inserting Eq. [3] into an equation of the form

$$N_p = \int_{a_{eff}}^{a_c} \frac{da}{f(\Delta K)} \quad [4]$$

where  $N_p$  is the propagation lifetime for a specimen with an initial effective crack length of  $a_{eff}$  following impact damage and a critical flaw size to cause failure ( $a_c$ ). Figure 13 shows the stress-lifetime curves generated by numerically integrating the ATANH equation according to Eq. [4], for the 48-2-2 specimens damaged at 3000 N using  $\Delta K_{TH}$  data. Initial effective crack lengths of 400, 500, and 600  $\mu\text{m}$  were used for generating the curves, since they bound the measured effective crack lengths of the impacted specimens. The actual effective crack lengths for each specimen are identified for comparison with the generated curves. As Figure 13 indicates, the curves generated by Eq. [3] accurately bound the experimental data, indicating that at these crack sizes, long-crack behavior can be anticipated.

However, the ATANH equation overestimated the experimentally measured fatigue strengths of specimens impacted at 1000 N ( $a_{eff} \approx 75 \mu\text{m}$ ), even if crack closure is taken into consideration. The lower-than-predicted endurance limit for specimens indented at 1000 N suggests growth at  $\Delta K$  values below  $\Delta K_{TH}$  or  $\Delta K_{eff,TH}$ .

To accommodate this behavior, the ATANH equation was constrained to model the closure-corrected, long-crack fatigue-crack-growth data ( $\Delta K_{eff}$ ) shown in Figure 10, with an artificial threshold stress-intensity range of 3.3  $\text{MPa}\sqrt{\text{m}}$ . The results of this regression are shown in Figure 14. The resulting curve fit exhibits a small-crack threshold in combination with the asymptotic near-threshold behavior represented by the ATANH equation.

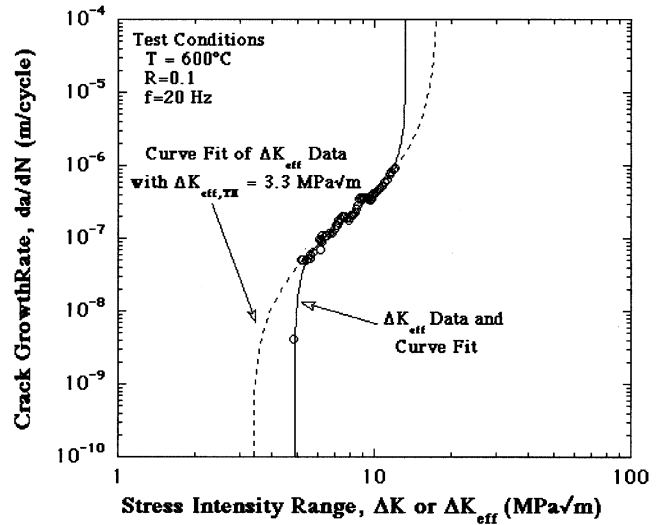


Fig. 14—Data regression using the ATANH model for the 48-2-2 alloy tested at 600 °C. A regression fit for the long-crack data is shown along with a fit artificially constrained to have a threshold of 3.3  $\text{MPa}\sqrt{\text{m}}$ .

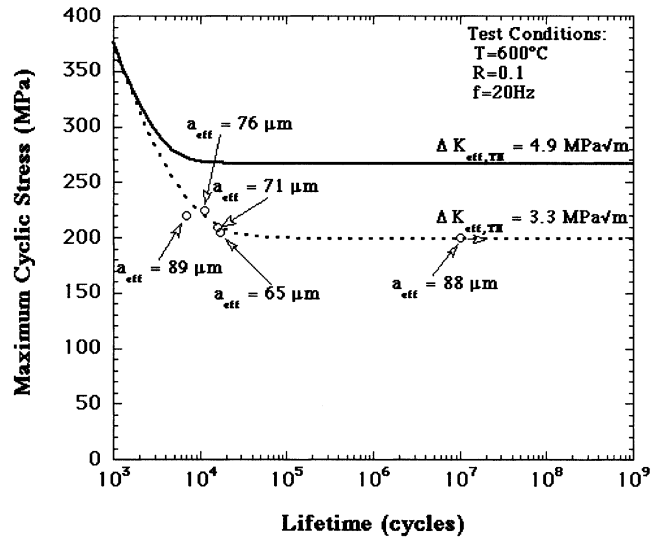


Fig. 15—Comparison of stress-lifetime curves calculated from the ATANH equation with  $\Delta K_{eff,TH}$  values of 4.9 and 3.3  $\text{MPa}\sqrt{\text{m}}$ . Use of the lower threshold value results in good estimation of both the endurance limit and short lifetime behavior of specimens with effective crack lengths on the scale of 75  $\mu\text{m}$ .

The stress-lifetime curves generated for an average effective crack length of 75  $\mu\text{m}$ , using Eq. [3] with and without the artificially constrained threshold of 3.3  $\text{MPa}\sqrt{\text{m}}$ , are shown in Figure 15. It is clear from the figure that the modified form of the ATANH equation not only accurately predicts the endurance limit of these small-crack specimens, but also represents their behavior at shorter lifetimes.

Figure 16 shows the Kitagawa plot for 48-2-2, comparing the long-crack  $\Delta K_{TH}$  and  $\Delta K_{eff,TH}$  prediction lines with a prediction line from the small-crack threshold of 3.3  $\text{MPa}\sqrt{\text{m}}$ . From the figure, it can be seen that the new threshold line accurately predicts the fatigue strength of specimens with effective crack lengths on the order of 75  $\mu\text{m}$ , as determined from step tests. However, the fatigue

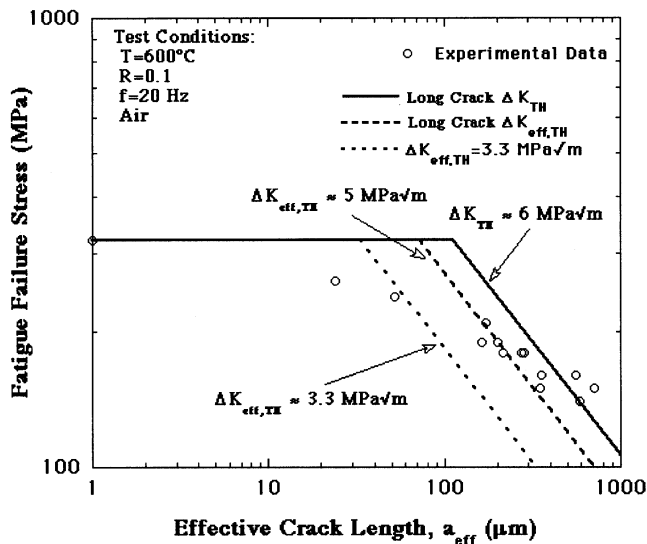


Fig. 16—Modified Kitagawa plot with an additional threshold prediction line for the arbitrary value of  $\Delta K_{\text{eff,TH}} = 3.3 \text{ MPa}\sqrt{\text{m}}$ . The new threshold line provides a good estimate of cracks on the order of  $75 \mu\text{m}$ , but still overestimates the strength of even less severe damage.

strengths of specimens with even smaller effective crack lengths are still lower than either this small-crack threshold or the fatigue strength of undamaged material. For design, a small-crack threshold of  $3.3 \text{ MPa}\sqrt{\text{m}}$  would appear to be inappropriate. However, if the fatigue strength of undamaged material is to be reduced by a factor of safety, this fatigue threshold value may be suitable.

It is worth noting that the threshold stress-intensity range of  $3.3 \text{ MPa}\sqrt{\text{m}}$  was arbitrarily chosen to produce the best fit of the measured endurance limit using the ATANH equation. However, Larsen *et al.*<sup>[41]</sup> found that a threshold stress-intensity-range value of  $3.3 \text{ MPa}\sqrt{\text{m}}$  could be used to predict the behavior of specimens from a lamellar  $\gamma$ -TiAl alloy that were notched by EDM. The notches were roughly  $80\text{-}\mu\text{m}$  deep in a material with a lamellar colony size of approximately  $760 \mu\text{m}$ .<sup>[42]</sup> They found that the experimental endurance limit could be predicted by using a threshold of  $3.3 \text{ MPa}\sqrt{\text{m}}$ , well below  $\Delta K_{\text{eff,TH}}$ , in Eq. [2]. This value was identified by Yokoshima and Yamaguchi<sup>[43]</sup> as the lower limit of the fracture toughness of polysynthetically twinned (PST) crystals of a lamellar  $\gamma$ -TiAl when the lamellar plates are oriented perpendicular to the loading axis. The correlation between the stress-lifetime results in duplex 48-2-2 following impacts at 1000 N and a value for the minimum toughness of PST crystals may be coincidental. However, it indicates that the use of a very conservative fatigue threshold for realistic life prediction of small cracks in damaged  $\gamma$ -TiAl may be valid. Moreover, it points to the need for a more complete understanding of the effects of local microstructural features on the threshold stress intensity of cracks resulting from low-severity impacts.

#### IV. CONCLUSIONS

1. Step-loading fatigue tests on a Ti-47.9Al-2.0Cr-1.9Nb duplex alloy and a Ti-47.3Al-2.2Nb-0.6Mn-0.45W-0.46Mo-0.23Si near-fully lamellar alloy have shown that a threshold-based approach can be used to predict the

effect of simulated assembly-related impact damage on the fatigue strength. However, a greater understanding of the effects of small cracks, residual stresses, and crack shape may be required if fatigue-critical components are to be designed from  $\gamma$ -TiAl.

2. A regression fit of long-crack fatigue-crack growth-rate behavior was successfully used to model the  $600 \text{ }^\circ\text{C}$  stress-lifetime response of the Ti-47.9Al-2.0Cr-1.9Nb duplex alloy following severe impacts. However, the small-crack effect observed for lightly damaged specimens of the same alloy could only be modeled by including a fatigue-crack-growth threshold value considerably lower than that used for long cracks. This reinforces the need to establish a small-crack threshold as a lower bound for design. Such a conservatively low threshold may, in the end, eliminate the need to adjust the threshold-based model for any potential residual-stress and/or crack-shape effects.
3. Fractographic analysis suggests that the true nature of the simulated damage studied here may fall somewhere between a through-thickness crack assumption and a corner-crack assumption, and fatigue threshold models based on these two crack shapes may serve as lower and upper bounds, respectively, of the actual behavior.

#### ACKNOWLEDGMENTS

Funding for this work was provided by the Air Force Office of Scientific Research under Grant No. F49620-95-1-0359. The valuable contributions of Drs. James Larsen and Andrew Rosenberger, Air Force Research Laboratory at Wright-Patterson AFB, are gratefully acknowledged. The authors also thank Dr. Paul Steif and Mr. Volus McKenna, Carnegie Mellon University, as well as Dr. Tresa Pollock, University of Michigan, for their insights on impacts and gamma titanium aluminide alloys.

#### REFERENCES

1. I.J. Perrin: *Gas Turbine Engine Technology: Proc. of 4th Int. Charles Parsons Turbine Conf.*, 1998, Institute of Metals, London, pp. 148-158.
2. C.M. Austin, T.J. Kelly, K.G. McAllister, and J.C. Chesnutt: *Structural Intermetallics*, M.V. Nathal, R. Darolia, C.T. Liu, P.L. Martin, D.B. Miracle, R. Wagner, and M. Yamaguchi, eds., TMS, Warrendale, PA, 1997, pp. 413-25.
3. S.C. Huang and J.C. Chesnutt: *Intermetallic Compounds: Vol. 2, Practice*, J.H. Westbrook and R.L. Fleischer, eds., John Wiley and Sons, New York, NY, 1993, pp. 379-81.
4. J.P. Campbell, K.T. Venkataswara Rao, and R.O. Ritchie: *Mater. Sci. Eng. A*, 1997, vols. 239-240, pp. 722-28.
5. A.H. Rosenberger, B.D. Worth, and S.J. Balsone: *Fatigue '96 Proc. 6th Int. Fatigue Congr. Vol. III*, G. Lütjering and H. Nowack, eds., Pergamon Press, Elmsford, NY, 1996, pp. 1785-90.
6. K. Sadananda and A.K. Vasudevan: *Mater. Sci. Eng. A*, 1995, vols. 192-193, pp. 490-501.
7. K.T. Venkataswara Rao, Y.-W. Kim, C.L. Muhlstein, and R.O. Ritchie: *Mater. Sci. Eng. A*, 1995, vols. 192-193, pp. 474-82.
8. B.A. Lerch, S.L. Draper, G.Y. Baaklini, and J.M. Pereira: *HITEMP Review 1999: Advanced High Temperature Engine Materials Technology Project*, NASA CP 1999-208915, NASA, vol. 2, pp. 30-1-30-11.
9. O. Roders, J.O. Peters, A.W. Thompson, and R.O. Ritchie: *Proc. of 4th Nat. Turbine Engine HCF Conf.*, Universal Technology Corp., Dayton, OH, 1999.
10. T. Nicholas, J.P. Barber, and R.S. Bertke: *Exp. Mech.*, 1980, vol. 20 (10), pp. 357-64.
11. S.J. Hudak, Jr., C.G. Chell, T.S. Rennick, R.C. McClung, and D.L. Davidson: *Proc. 4th Nat. Turbine Engine HCF Conf.*, Universal Technology Corp., Dayton, OH, 1999, in press.

12. S.C. Huang: U.S. Patent 5,076,858, 1991.
13. C. Austin: General Electric Aircraft Engines, Cincinnati, OH, unpublished research, 1995.
14. J. LaSalle: Allison Engines, Morristown, NJ, unpublished research, 1997.
15. K.S. Chan and Y.-W. Kim: *Metall. Trans. A*, 1993, vol. 24A, pp. 113-25.
16. J. Kumpfert, Y.-W. Kim, and D.M. Dimiduk: *Mater. Sci. Eng. A*, 1995, vols. 192-193, pp. 465-73.
17. J.A. Collins: *Failure of Materials in Mechanical Design*, John Wiley and Sons, New York, NY, 1993, pp. 379-81.
18. E.J. Dolley, N.E. Ashbaugh, and B.D. Worth: *Fatigue '96: Proc. 6th Int. Fatigue Congr. Vol. III*, G. Lütjering and H. Nowack, eds., Pergamon Press, Elmsford, NY, 1996.
19. T.S. Harding and J.W. Jones: *Metall. Mater. Trans. A*, 2000, vol. 31A, pp. 1741-52.
20. P.S. Steif, V.T. McKenna, J.W. Jones, R. Smith, T.S. Harding, and A. Gilchrist: *Proc. 3rd Int. Symp. on Structural Intermetallics*, The Minerals, Metals and Materials Society, Warrendale, PA, 2001, pp. 363-70.
21. T.M. Pollock, D.R. Mumm, K. Muraleedharan, and P.L. Martin: *Scripta Mater.*, 1996, vol. 35 (11), pp. 1311-16.
22. M.P. Rubal and P.S. Steif: *PRET: A University-Industry Partnership for Research and Transition of Gamma Titanium Aluminides Annual Report*, Carnegie Mellon University, Pittsburgh, PA, Sept. 1997.
23. R. Gnanamoorthy, Y. Mutoh, K. Hayashi, and Y. Mizuhara: *Scripta Metall. Mater.*, 1995, vol. 33, pp. 907-12.
24. D.L. Davidson and J.B. Campbell: *Metall. Trans. A*, 1993, vol. 24A, pp. 1555-74.
25. P. Bowen, R.A. Chave, and A.W. James: *Mater. Sci. Eng. A*, 1995, vols. 192-93, pp. 443-56.
26. H. Shiota, K. Tokaji, and Y. Ohta: *Mater. Sci. Eng. A*, 1998, vol. 243, pp. 169-75.
27. K.S. Chan and Y.-W. Kim: *Metall. Trans. A*, 1992, vol. 23, pp. 1663-77.
28. K.S. Chan: *Metall. Trans. A*, 1993, vol. 24, pp. 569-83.
29. T.S. Harding, J.W. Jones, P.S. Steif, and T.M. Pollock: *Scripta Mater.*, 1999, vol. 4 (4), pp. 445-49.
30. Y.-W. Kim: *JOM*, 1994, vol. 46 (7), pp. 30-39.
31. S.J. Trail and P. Bowen: *Mater. Sci. Eng. A*, 1995, vols. 192-193, pp. 427-34.
32. H. Kitagawa and S. Takahashi: *Proc. 2nd Int. Conf. on Mechanical Behavior of Metals*, Boston, MA, 1976, pp. 627-31.
33. T.S. Harding and J.W. Jones: *Scripta Mater.*, 2000, vol. 43, pp. 623-29.
34. W.F. Brown, Jr. and J.E. Srowley: *Plane Strain Crack Toughness Testing of High Strength Metallic Materials*, ASTM STP 410, 1966, p. 12.
35. B.D. Worth and J.M. Larsen: Materials Directorate, Wright Patterson Air Force Base, OH, unpublished research, 1997.
36. K. Tanaka, Y. Nakai, and M. Yamashita: *Int. J. Fract.*, 1981, vol. 17, pp. 519-33.
37. M.H. ElHaddad, N.F. Dowling, T.H. Topper, and K.N. Smith: *Int. J. Fract.*, 1980, vol. 16, p. 15.
38. D. Taylor: *Fatigue Thresholds*, Butterworth Publishing, London, 1989, pp. 132-57.
39. J.M. Larsen, B.D. Worth, S.J. Balsone, and A.H. Rosenberger: *Proc. 8th World Conf. on Titanium*, Birmingham, United Kingdom, 1995, D.A. Blenkinsop, W.J. Evans, and H.M. Flower, eds., Institute of Metals, London, 1996, pp. 113-20.
40. J.M. Larsen, B.D. Worth, C.G. Annis, Jr., and F.K. Haake: *Int. J. Fract.*, 1996, vol. 80, pp. 237-55.
41. J.M. Larsen, A.H. Rosenberger, B.D. Worth, K. Li, D.C. Maxwell, and J.W. Porter: in *Gamma Titanium Aluminides 1999*, 1999, Y.-W. Kim, D.M. Dimiduk, and M.H. Loretto, eds., TMS, Warrendale, PA, 1999, pp. 463-72.
42. S.J. Balsone, J.M. Larsen, D.C. Maxwell, and J.W. Jones: *Mater. Sci. Eng. A*, 1995, vols. 192-193, pp. 457-64.
43. S. Yokoshima and M. Yamaguchi: *Acta Mater.*, 1996, vol. 44 (3), pp. 873-83.